

Graphene cantilever beams for nano switches

Cite as: Appl. Phys. Lett. **101**, 093111 (2012); <https://doi.org/10.1063/1.4738891>

Submitted: 04 January 2012 . Accepted: 09 July 2012 . Published Online: 31 August 2012

Peng Li, Zheng You, and Tianhong Cui



View Online



Export Citation

ARTICLES YOU MAY BE INTERESTED IN

[Suspended few-layer graphene beam electromechanical switch with abrupt on-off characteristics and minimal leakage current](#)

Applied Physics Letters **99**, 023103 (2011); <https://doi.org/10.1063/1.3610571>

[All graphene electromechanical switch fabricated by chemical vapor deposition](#)

Applied Physics Letters **95**, 183105 (2009); <https://doi.org/10.1063/1.3259415>

[Low pull-in voltage graphene electromechanical switch fabricated with a polymer sacrificial spacer](#)

Applied Physics Letters **105**, 033103 (2014); <https://doi.org/10.1063/1.4891055>

Lock-in Amplifiers up to 600 MHz

starting at

\$6,210



Zurich Instruments

Watch the Video

AIP
Publishing

Graphene cantilever beams for nano switches

Peng Li,^{1,2} Zheng You,^{1,a)} and Tianhong Cui^{1,2,b)}

¹Department of Precision Instruments and Mechanology, State Key Laboratory of Precision Measuring Technology and Instruments, Tsinghua University, Beijing 100084, People's Republic of China

²Department of Mechanical Engineering, University of Minnesota, Minneapolis, Minnesota 55455, USA

(Received 4 January 2012; accepted 9 July 2012; published online 31 August 2012)

A method named sacrificial beam is presented to fabricate graphene cantilever devices. The mechanical properties of graphene cantilevers are studied using atomic force microscopy. Graphene cantilever based 2-terminal nano-electro-mechanical systems switches are demonstrated, and their DC characteristics and switch performance are investigated. A 3-terminal switch based on a graphene cantilever is fabricated, and its electrical properties are also studied. © 2012 American Institute of Physics. [<http://dx.doi.org/10.1063/1.4738891>]

Graphene, initially generated by Novoselov *et al.*,¹ is a two-dimensional honeycomb crystal of carbon atoms, and has very unique electrical and mechanical properties. The high carrier mobility of graphene (200 000 cm²/Vs (Ref. 2) makes it an ideal candidate for future microelectronic applications.^{3–11} Its thermal conductivity is 5000 W/mK,¹² and its Young's modulus is about 1 TPa,¹³ at least six times higher than silicon, making it an excellent material for nanoelectromechanical systems (NEMS).^{14–17} Two-end-fixed beams and cantilevers are two important types of NEMS structures, and the latter one may have more potential applications due to its linear behavior and high sensitivity. Graphene beams have been extensively studied since 2007,^{18–23} however, to date, graphene cantilever device has not been reported because it is very challenging to fabricate graphene cantilevers. Compared with a two-end-fixed beam, making free-standing graphene cantilever is much more difficult. In this paper, we present a sacrificial beam (SB) approach, demonstrating a NEMS switch using this method.

The fabrication process, as shown in Figure 1, starts with depositing C_r/A_u/T_i (10 nm/100 nm/10 nm) by electron-beam evaporation on top of S_i substrate. C_r and T_i work as the bottom and top adhesion layers, respectively. T_i can be removed together with S_iO₂ by wet etching process using buffered oxide etchant (BOE). Therefore, graphene cantilevers can electrically in contact with the A_u layer with a good conductivity. Sequentially, 300 nm S_iO₂ was deposited on top of metal layers by plasma enhanced chemical vapor deposition (PECVD) as an isolation layer. Next, we used mechanical exfoliation method to transfer graphene on S_iO₂. The sequential electrodes fabrication involves photolithography, C_r/A_u electron-beam evaporation, and metal lift-off. We used PECVD to grow amorphous silicon approximately 300 nm thick on the sample, and used photolithography and SF₆ dry etching to pattern it to ensure that the amorphous silicon beam covers the graphene flake. The sample was rinsed in BOE to etch S_iO₂ and T_i layers, followed by a critical point drying. The function of amorphous silicon beam, as the SB, is to keep graphene to suspend during the wet etching process.

Figure 2(c) shows a free-standing amorphous silicon beam with graphene cantilever attached on its lower surface. After wet etching, we used SF₆ dry etching to remove the SB, leaving only suspended graphene cantilever. After SF₆ dry etching, no obvious damage on graphene cantilevers was observed. A prominent D peak was noticed in Raman spectrum (see Figure 2(e)) which indicates that the dry etching may introduce defects in graphene. These defects were caused by physical ion milling instead of chemical etching. Figure 2(a) is a scanning electron microscopy (SEM) image of a free-standing graphene cantilever arrays. As a comparison, we tried conventional BOE wet etching method. Without the SB, it is impossible to keep thin graphene cantilevers suspended after transferring it from one solution to another several times (see Figure 2(b)). Since graphene is very thin, it may curve after the SB is removed due to the built-in stress. Figure 2(d) shows a graphene 1 nm thick which was bended upward. Even with the amorphous silicon beam, some graphene cantilevers still collapsed onto the substrate after dry etching due to large length/thickness ratios. According to our experimental results, when the length/thickness ratio (l/t) is larger than 560, keeping graphene cantilever suspended is very challenging (see Figure 2(f)).

Mechanical properties of a graphene cantilever were investigated by atomic force microscopy (AFM). To have a better understanding of the width effect, we chose a graphene cantilever with a large width/length ratio. A multimodal AFM was used to acquire topographic images (Figure 3(a)) and collect force-Z curves in a 64 by 64 grid of locations (also called "force volume") for mechanical assessments. Dynamic mode instead of contact mode was chosen for high-resolution topographic imaging to minimize the tip's shear interaction with the delicate structure to avoid damage. Importantly, cantilever driving parameters were chosen to place the oscillator in the net *attractive* regime during dynamic mode imaging (dominated by van der Waals attraction instead of repulsive contact), as monitored via the phase signal. For mechanical measurements, the tip and beam sample were brought together so that the vertical oscillation of the AFM cantilever reduced to zero, and quasistatic contact was achieved between the tip and the beam. During indentation, the graphene cantilever was bended, and force against the sheet also caused AFM cantilever to deflect. The

^{a)}E-mail: yz-dpi@mail.tsinghua.edu.cn.

^{b)}Telephone: 1-612-626-1636. E-mail: tcui@me.umn.edu.

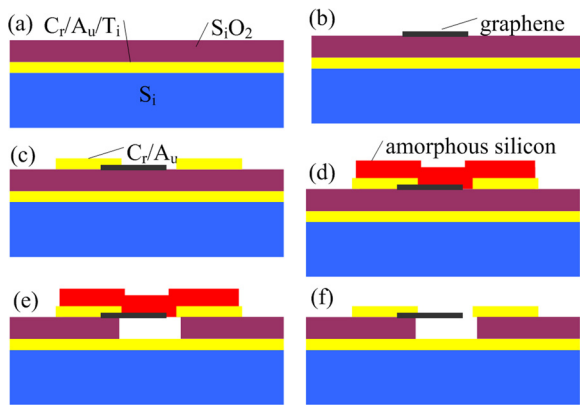


FIG. 1. Graphene cantilever fabrication process. (a) Deposit Cr/Au/Ti on Si substrate, followed by SiO₂ deposition. (b) Transfer mechanically exfoliated graphene on substrate. (c) Fabricate electrode pads on graphene by lift-off technique. (d) Deposit amorphous silicon on graphene and use SF₆ to pattern it. (e) Etch SiO₂ and Ti layer by using BOE. (f) Use SF₆ to remove SB.

relationship among the graphene cantilever displacement, $Z_{cantilever}$, the piezo stage movement (beneath sample), Z_{piezo} , and the AFM cantilever deflection, Z_{tip} , is

$$Z_{cantilever} = Z_{piezo} - Z_{tip}. \quad (1)$$

The force, F , applied to the graphene can be derived by

$$F = K_{tip}Z_{tip}, \quad (2)$$

where K_{tip} is the spring constant of a calibrated AFM cantilever. The force- Z data cube provided a 2D mapping of local stiffness. It provides us with sufficient information about the stiffness distribution. Figure 3(b) shows 4 force curves

derived from different positions described in the AFM height image. Spot 1 was the curve from the rigid electrode with the largest slope and was used as a reference to calibrate the sensitivity of the AFM cantilever deflection. Spot 2 has smaller stiffness than spot 3, corresponding to a less slope in a force curve. Spot 4 is the softest position of the cantilever. In addition, the force curves imply that a graphene cantilever is a linear system. In pure bending regime, the relationship between force and displacement of a cantilever under concentrated force is given by

$$F = \frac{Ewt^3}{4l^3}Z_{cantilever}, \quad (3)$$

where E is the graphene Young's modulus, l , w , and t are length, width, and thickness of the graphene cantilever, respectively. The Young's modulus of 0.7 TPa and 0.8 TPa was deduced from force curves 2 and 3, respectively. 0.8 TPa is a more reasonable result inasmuch as there is no edge effect while indenting spot 3. Two factors mainly contribute to the measurement error of Young's modulus. The measurement error of AFM cantilever's spring constant is within $\pm 10\%$, and the measurement of the graphene's thickness with error about ± 0.2 nm. Therefore, the Young's modulus of graphene is about 0.8 ± 0.09 TPa.

2-terminal graphene cantilever NEMS switches electro-mechanically actuated are demonstrated and analyzed. The top graphene film can be pulled down to be in contact with the A_u substrate electrically when applying a dc voltage on the top (graphene) and bottom (A_u) electrodes. Once the bias is larger than the pull-in voltage, a sharp increase of the current is observed, implying that the top graphene cantilever is

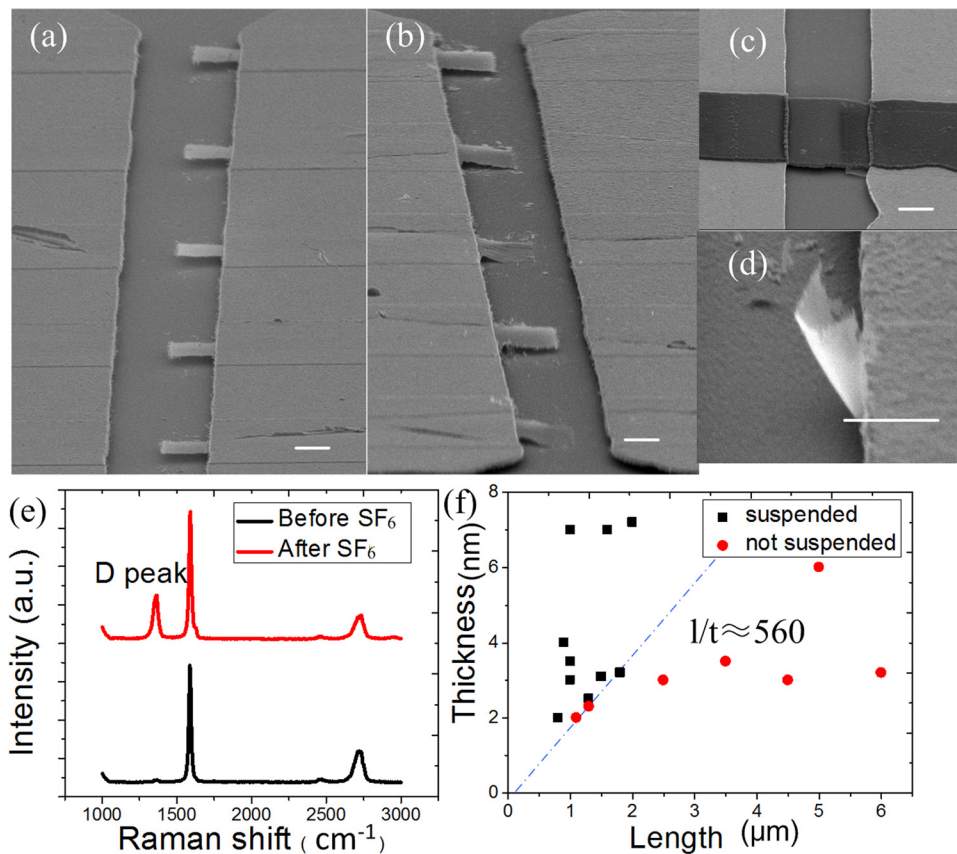


FIG. 2. Graphene cantilever. (a) SEM image of graphene cantilever arrays. (b) Graphene cantilevers which fabrication do not involve SB. (c) SEM image of a free-standing amorphous silicon beam with graphene cantilever attached on its lower surface. (d) A 1-nm-thick graphene cantilever. (e) Raman spectra of graphene cantilever before and after SF₆ etching. (f) The relation between suspension and graphene cantilever's length/thickness ratio. The scale bar is 1 μ m.

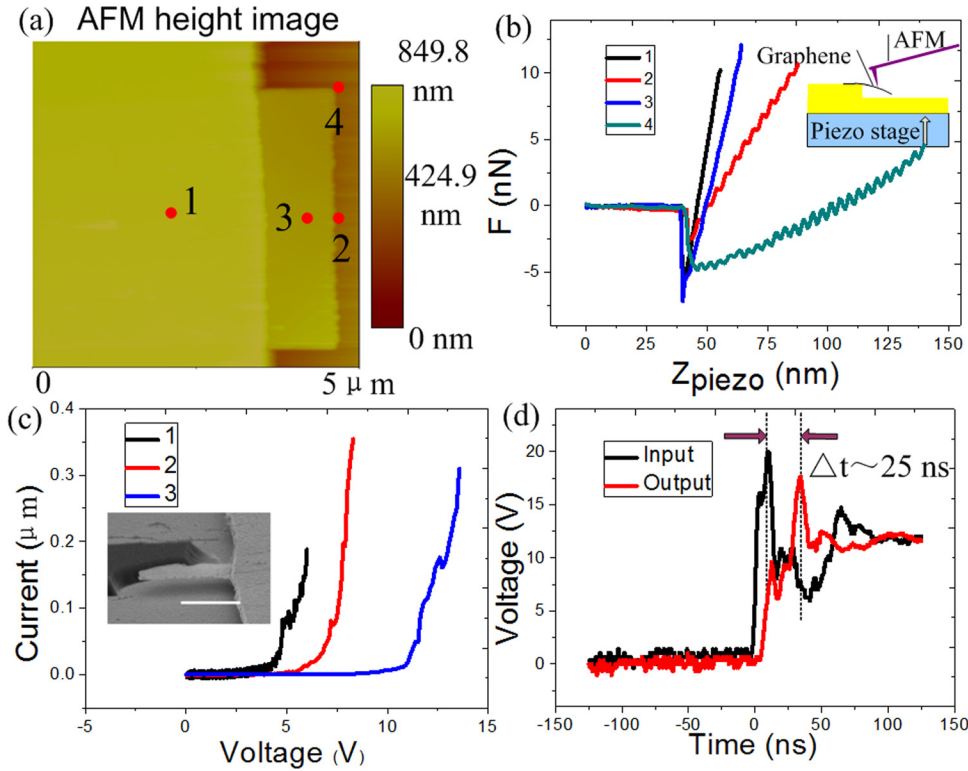


FIG. 3. (a) AFM topographic image of a graphene cantilever. (b) Force curves of graphene cantilever. 4 curves are derived from the different positions described in (a). Inset shows a schematic view of AFM indentation. (c) I-V measurement of 3 different graphene cantilevers. A dc voltage was applied on the top (graphene) and bottom (A_u) electrodes. Once the bias was larger than the pull-in voltage, and a sharp increase of the current was observed. The inset is the SEM image of a graphene cantilever beam after switching which is still suspended. The scale bar is $1 \mu\text{m}$. (d) Input and output waveforms of graphene cantilever switch. The difference in time needed to reach the maximum voltage between the two signals was approximately 25 ns, which is the delay time.

in contact with the bottom, and the switch is turned on. The contact, 12 out of 19 cantilevers, is broken after the bias is removed (one is shown in Figure 3(c)). Cantilevers larger than 2 nm thick stand a much smaller chance to have stiction failure after switching.

The spring constant of a cantilever under distribution force is given by

$$k = \frac{2Ew}{3} \left(\frac{t}{l}\right)^3. \quad (4)$$

Thus, the pull-in voltage is given by²⁴

$$V_{\text{pull-in}} = \sqrt{\frac{8kg_0^3}{27\varepsilon lw}} = \sqrt{\frac{16Et^3g_0^3}{81\varepsilon l^4}}, \quad (5)$$

where g_0 is the air gap between graphene and A_u , and ε is vacuum permittivity. In our experiments, the currents were measured as a function of dc bias voltage. Figure 3(c) shows the I-V curves of 3 cantilever switches in the same length of $1 \mu\text{m}$. Cantilevers 1 and 2 have the same thickness of 4 nm, but cantilever 1 is wider ($4 \mu\text{m}$) than 2 ($2.5 \mu\text{m}$). When the dc voltage is increased, spot 4 in Figure 3(a) will be pulled down first. Wider cantilever has softer edge, resulting in smaller pull-in voltages. Graphene cantilever in device 3 is thicker (6 nm), thus larger actuation voltage was needed. If the cantilever is narrow (width less than $2 \mu\text{m}$), the difference between measured pull-in voltage and the value predicted by Eq. (5) is within 10%, otherwise the measured value is smaller due to the edge effect mentioned above.

The switching speed measurement is also conducted. For electromechanically actuated switches, the switching time consists of the response time, which is the time needed to overcome mechanical inertia, and the rise time of the voltage due to capacitance charging. A step function was applied

to the device input terminal, and the output signal was measured across a resistor in series to ground. In order to compare the waveform difference in time domain, both the input and output signals were displayed on the same digital oscilloscope synchronously. When an input voltage of 10 V was applied, we observed a pulse output signal, as shown in Figure 3(d). The oscillations in the input and switch output waveforms may arise from resonance associated with the inductance and the capacitance from the instrumentation. The different time needed to reach the maximum voltage between the two signals was approximately 25 ns, which is the delay time and also an upper bound of the intrinsic switching speed of our graphene cantilever switch. The switching time, t , is given by²⁴

$$t = \frac{3.67V_{\text{pull-in}}}{2\pi f_0 V}, \quad (6)$$

where V is the step function voltage, and f_0 is the first order resonant frequency of cantilever. The switching time, t , derived from Eq. (6) is 17 ns, which is in the same order of the delay time we measured. The difference is mainly caused by air damping.

In addition to 2-terminal switch which is easier to fabricate for initial research, we also fabricate and characterize 3-terminal switches for further investigation. Two terminals are located on the signal transmission line (source and drain), and the third terminal (gate) is used to turn on/off the switch. We developed a 3-terminal graphene cantilever with the similar fabrication procedure, as shown in Figures 4(a)–4(d). First, we deposited $C_r/A_u/T_i$ on a S_iO_2/S_i substrate, and used photolithography, BOE, GE-6 A_u etchant, and CR-12 R C_r etchant to pattern T_i , A_u , and C_r , respectively. Sequentially, PECVD was used to deposit 300 nm S_iO_2 on top (see Figure 4(a)).

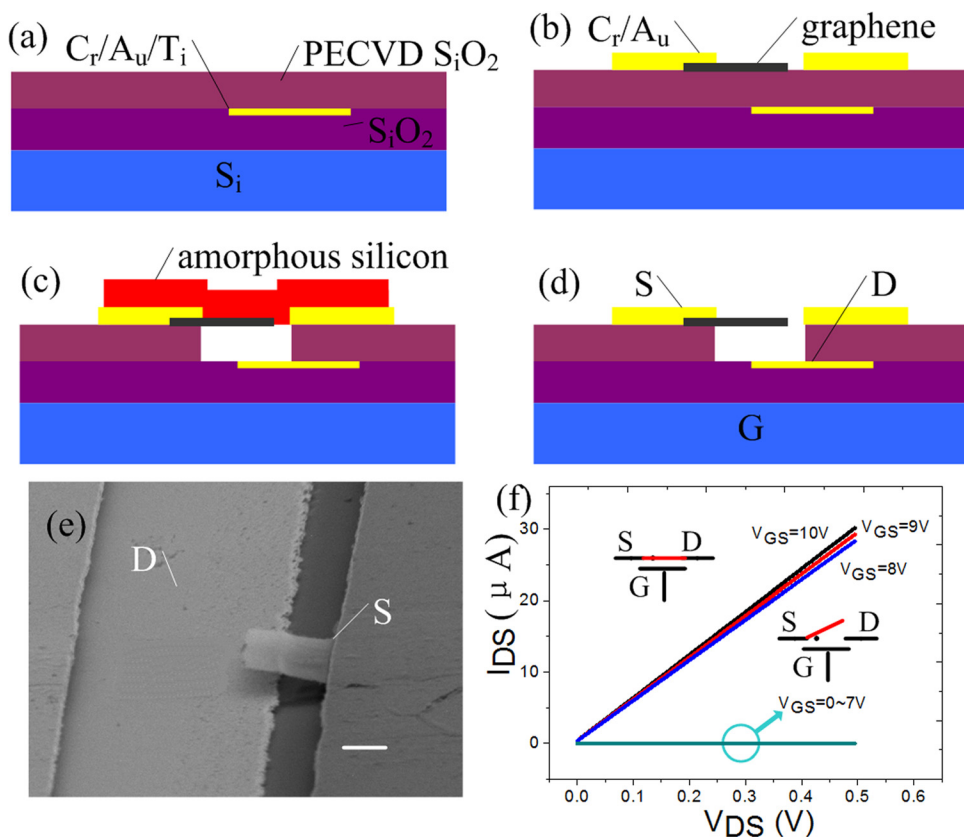


FIG. 4. 3-terminal graphene switch. (a)–(f) Fabrication process. (a) Deposit and pattern $C_r/A_u/T_i$ layers on SiO_2/Si substrate. Use PECVD to grow a layer of SiO_2 on top. (b) Transfer graphene on SiO_2 followed by electrodes fabrication. (c) Deposit amorphous silicon on graphene and use SF_6 to pattern it. Rinse sample in BOE to etch SiO_2 and T_i layer. (d) Use SF_6 to remove SB. (e) SEM image of a 3-terminal nano-switch based on graphene cantilever. (f) I-V curves of 3-terminal switch. The scale bar is $1 \mu m$.

After using mechanical exfoliation to transfer graphene on SiO_2 , we chose graphene flakes located on top of the $C_r/A_u/T_i$ pattern edge and fabricate the top electrodes (see Figure 4(b)). Finally, the SB technique was used to make graphene cantilever suspended. Figure 4(e) is a SEM image of a 3-terminal graphene cantilever switch. We define graphene, intermediate metal layer, and the conductive silicon substrate as S, D, and G, respectively. Voltages of V_{GS} and V_{DS} are applied to the device. When V_{GS} is smaller than the pull-in voltage, no current is observed between S and D ($I_{DS} = 0$). Once V_{GS} reaches 8 V, the graphene cantilever is pulled to be in contact with D electrically. Consequently, I_{DS} largely increases, indicating the switch is turned on (see Figure 4(f)). The 3-terminal switch is reversible. The contact is broken after the bias is removed.

In summary, a method SB is reported to fabricate graphene cantilevers. The mechanical properties of graphene cantilevers are studied by AFM indentation, and the Young's modulus of graphene, 0.8 TPa, is derived from indentation force curves. We demonstrate 2-terminal graphene cantilever RF switches with their dc characteristics and switching speed investigated. 3-terminal switch is also developed, and its electrical properties are studied. In addition, we believe that the graphene cantilever is likely to be a good platform for various types of NEMS sensors and actuators. As a sensor, it has better sensitivity than the two-end-fixed beam with the same dimensions. The high sensitivity of micro-scale cantilever has been discussed in many papers. For example, the development of micro-fabricated cantilevers for AFM signified an important milestone in MEMS sensors.²⁵ As an actuator, it can take advantage of the linear relationship between the actuation force and the displacement with a very high Young's modu-

lus. The linearity of graphene cantilever has been proved by AFM indentation in this paper. Therefore, compared with graphene two-end-fixed beam, it may have more potential applications to MEMS and NEMS.

The authors acknowledge the assistance of fabrication and characterization from the Nanofabrication Center and the Characterization Facility at the University of Minnesota.

- ¹K. S. Novoselov, A. K. Geim, S. V. Morozov, D. Jiang, Y. Zhang, S. V. Dubonos, I. V. Grigorieva, and A. A. Firsov, *Science* **306**, 666 (2004).
- ²X. Du, I. Skachko, A. Barker, and E. Andrei, *Nat. Nanotechnol.* **3**, 491 (2008).
- ³X. Li, X. Wang, L. Zhang, S. Lee, and H. Dai, *Science* **319**, 1229 (2008).
- ⁴Y. M. Lin, C. Dimitrakopoulos, K. A. Jenkins, D. B. Farmer, H. Y. Chiu, A. Grill, and P. Avouris, *Science* **327**, 662 (2010).
- ⁵F. Schwierz, *Nat. Nanotechnol.* **5**, 487 (2010).
- ⁶Y. Zhang, T. T. Tang, C. Girit, Z. Hao, M. C. Martin, A. Zettl, M. F. Crommie, Y. R. Shen, and F. Wang, *Nature (London)* **459**, 820 (2009).
- ⁷J. Oostinga, H. B. Heersche, X. Liu, A. F. Morpurgo, and L. M. K. Vandersypen, *Nature Mater.* **7**, 152 (2008).
- ⁸Y. M. Lin, K. A. Jenkins, A. V. Garcia, J. P. Small, D. B. Farmer, and P. Avouris, *Nano Lett.* **9**, 422 (2009).
- ⁹S. Bae, H. Kim, Y. Lee, X. Xu, J. S. Park, Y. Zheng, J. Balakrishnan, T. Lei, H. R. Kim, Y. Song, Y. J. Kim, B. H. Hong, and S. Lijima, *Nat. Nanotechnol.* **5**, 574 (2010).
- ¹⁰J. T. Robinson, F. K. Perkins, E. S. Snow, Z. Wei, and P. E. Sheehan, *Nano Lett.* **8**, 3137 (2008).
- ¹¹X. Liang, A. S. P. Chang, Y. Zhang, B. D. Harteneck, H. Choo, D. L. Olynick, and S. Cabrini, *Nano Lett.* **9**, 467 (2009).
- ¹²A. A. Balandin, S. Ghosh, W. Bao, I. Calizo, D. Teweldebrhan, F. Miao, and C. N. Lau, *Nano Lett.* **8**, 902 (2008).
- ¹³C. Lee, X. Wei, J. W. Kysar, and J. Hone, *Science* **321**, 385 (2008).
- ¹⁴J. S. Bunch, A. M. V. Zande, S. S. Verbridge, L. W. Frank, D. M. Tanenbaum, J. M. Parpia, H. G. Craighead, and P. L. McEuen, *Science* **315**, 490 (2007).
- ¹⁵C. Chen, S. Rosenblatt, K. I. Bolotin, W. Kalb, I. Kymissis, H. L. Stormer, T. F. Heinz, and J. Hone, *Nat. Nanotechnol.* **4**, 861 (2009).

- ¹⁶K. M. Milaninia, M. A. Baldo, A. Reina, and J. Kong, *Appl. Phys. Lett.* **95**, 183105 (2009).
- ¹⁷S. Zhu, R. Shabani, J. Rho, Y. Kim, B. H. Hong, J. Ahn, and H. J. Cho, *Nano Lett.* **11**, 977 (2011).
- ¹⁸S. Shivaraman, R. A. Barton, X. Yu, J. Alden, L. Herman, M. Chandrashekar, J. Park, P. L. McEuen, J. M. Parpia, H. G. Craighead, and M. G. Spencer, *Nano Lett.* **9**, 3100 (2009).
- ¹⁹D. Garcia-Sanchez, A. M. Zande, A. S. Paulo, B. Lassagne, P. L. McEuen, and A. Bachtold, *Nano Lett.* **8**, 1399 (2008).
- ²⁰R. T. Weitz, M. T. Allen, B. E. Feldman, J. Martin, and A. Yacoby, *Science* **330**, 812 (2010).
- ²¹C. Seoanez and F. Guinea, *Phys. Rev. B* **76**, 125427 (2007).
- ²²S. Lee, N. Wijesinghe, C. Diaz-Pinto, and H. Peng, *Phys. Rev. B* **82**, 045411 (2008).
- ²³Z. Cheng, Q. Li, Z. Li, Q. Zhou, and Y. Fang, *Nano Lett.* **10**, 1864 (2010).
- ²⁴G. M. Rebeiz, *RF MEMS: Theory, Design, and Technology* (John Wiley & Sons, Hoboken, New Jersey, 2003).
- ²⁵G. Bing, C. F. Quate, and C. Gerber, *Phys. Rev. Lett.* **56**, 930 (1986).